2010

Seasonal Ice Cycle at the Mars Phoenix Landing Site: 2. Postlanding CRISM and Ground Observations

Selby Cull
Bryn Mawr College, scull@brynmawr.edu

R. E. Arvidson

R. V. Morris

M. Wolff

M. T. Mellon

See next page for additional authors

Custom Citation

Cull, S., R. E. Arvidson, R. V. Morris, M. Wolff, M. T. Mellon, and M. T. Lemmon (2010), Seasonal ice cycle at the Mars Phoenix landing site: 2. Postlanding CRISM and ground observations, *J. Geophys. Res.*, 115, E00E19, doi: 10.1029/2009JE003410.

Authors
Selby Cull, R. E. Arvidson, R. V. Morris, M. Wolff, M. T. Mellon, and M. T. Lemmon

Seasonal ice cycle at the Mars Phoenix landing site: 2. Postlanding CRISM and ground observations

Selby Cull,[1] R. E. Arvidson,[1] R. V. Morris,[2] M. Wolff,[3] M. T. Mellon,[4] and M. T. Lemmon[5]

Received 30 April 2009; revised 16 November 2009; accepted 7 January 2010; published 29 May 2010.

[1] The combination of ground observations from the Mars Phoenix Lander and orbital data from the Compact Reconnaissance Imaging Spectrometer for Mars (CRISM) provided a detailed view of the formation of late summer surface water ice at the landing site and surrounding regions. CRISM observations of the landing site during and immediately after Phoenix operations were analyzed to track the seasonal and diurnal ice cycles during the late spring to late summer, and a nonlinear mixing model was used to estimate grain sizes and relative abundances of water ice and dust. The surface around the Phoenix landing site was ice-free from late spring through midsummer, although transient patches of mobile ices were observed in an 85 m diameter crater to the northeast of the landing site. At the ~10 km diameter Heimdal Crater, located ~10 km east of the landing site, permanent patches of water ice were observed to brighten during the late spring and darken during the summer, possibly as fine-grained water ice that was cold trapped onto the ice during late spring sintered into larger grains or finally sublimated, exposing larger-grained ice. CRISM spectra first show evidence of widespread ice during the night at solar longitude (L_s) ~ 109°, ~9 sols before Phoenix's Surface Stereo Imager detected it. CRISM spectra first show evidence of afternoon surface ice and water ice clouds after L_s ~ 155°, after Phoenix operations ended.

Citation: Cull, S., R. E. Arvidson, R. V. Morris, M. Wolff, M. T. Mellon, and M. T. Lemmon (2010), Seasonal ice cycle at the Mars Phoenix landing site: 2. Postlanding CRISM and ground observations, *J. Geophys. Res.*, *115*, E00E19, doi:10.1029/2009JE003410.

1. Introduction

[2] The Mars Phoenix Lander touched down on 25 May 2008 at 68.22°N, 234.25°E (planetocentric) [*Arvidson et al.*, 2009], and operated on the surface from solar longitude (L_s) ~ 77° (late spring) to L_s ~ 149° (midsummer), when a combination of decreased solar radiation and a dust storm resulted in a mission-ending lack of power. One objective of the Phoenix mission was to characterize the northern high-latitude environment during the summer season, including the water ice and dust cycles [*Smith et al.*, 2008]. A complete understanding of the water cycle and environment is necessary for understanding mechanisms that relate to habitability, for example the migration of thin films of water and the exchange of water between the atmosphere and ice table. The water ice cycle has particular interest for Phoenix because the landing site is covered for much of the year by the seasonal ice cap: a layer of CO_2 and H_2O ices that extends from the north pole to ~50°N [*James et al.*, 1993; *Cull et al.*, 2010]. Phoenix observations of the onset of the seasonal ice cap, when combined with orbital observations, provide a detailed view of the seasonal ice cycle at the northern high latitudes of Mars.

[3] Previous studies have described the onset of the seasonal ice cap on a regional scale and have shown that cap development is spatially variable. *Kieffer and Titus* [2001] observed that by L_s ~ 162° the atmosphere is cold enough for water ice clouds to form north of ~64°N. They also noted that daytime surface temperatures north of ~68°N become cold enough for water frost to form between L_s ~ 164° and 184°. Based on Viking orbiter data, *Bass and Paige* [2000] estimated that water ice should be stable on the surface in the Phoenix latitude band as early as L_s ~ 155°. Given the considerable disagreement about the timing of ice appearance in this latitude band, it is difficult to pinpoint when water ice first appears at the Phoenix landing site using past data sets.

[4] *Cull et al.* [2010] used data from the Compact Reconnaissance Imaging Spectrometer for Mars (CRISM) onboard Mars Reconnaissance Orbiter (MRO) and High Resolution Imaging Science Experiment (HiRISE) to map

[1]Department of Earth and Planetary Sciences, Washington University in Saint Louis, Saint Louis, Missouri, USA.
[2]ARES, NASA Johnson Space Center, Houston, Texas, USA.
[3]Space Science Institute, Boulder, Colorado, USA.
[4]Laboratory for Atmospheric and Space Physics, University of Colorado, Boulder, Colorado, USA.
[5]Department of Atmospheric Science, Texas A&M University, College Station, Texas, USA.

0148-0227/10/2009JE003410

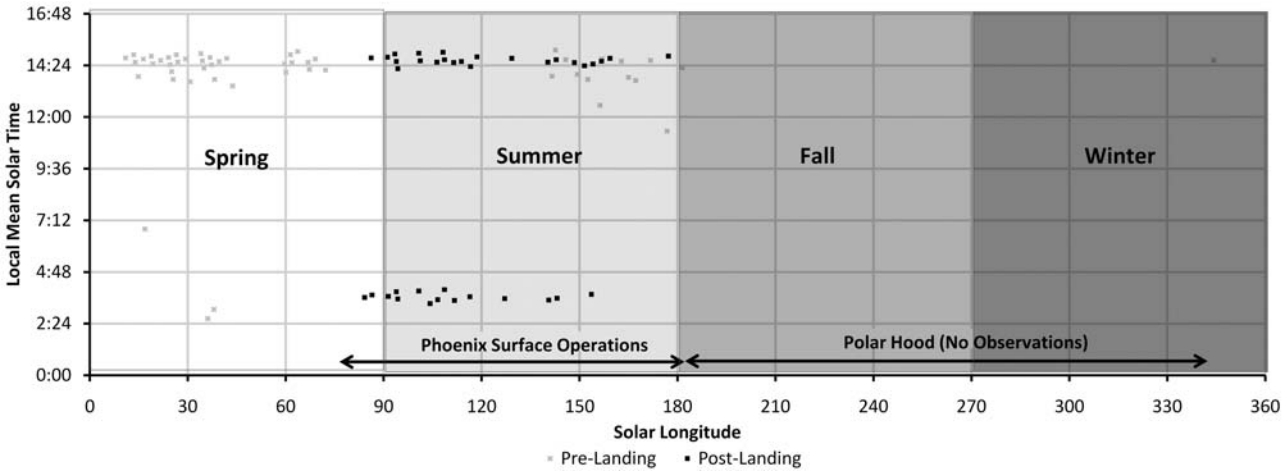

Figure 1. CRISM FRT observations over the Phoenix landing site. Gray squares are prelanding observations examined by *Cull et al.* [2010]. Black squares are postlanding observations examined here. All of the observations considered in this paper were taken either at 1300 LTST or 0300 LTST. No observations were taken between $L_s \sim 181°$ and 344° due to the presence of the polar hood.

seasonal ices from late summer to early spring, prior to Phoenix landing. In this paper, we examine the seasonal and diurnal ice cycles during and immediately after Phoenix operations, from late spring to late summer. High-resolution images and spectra from CRISM are used to identify water ice, and a nonlinear mixing model is used to estimate ice grain sizes and relative abundances. CRISM spectra at various viewing geometries are used to constrain surface scattering and physical properties. Finally, CRISM findings are compared to Phoenix ground measurements from the Surface Stereo Imager (SSI) [*Smith et al.*, 2008], lidar [*Whiteway et al.*, 2009], and Optical Microscope (OM) [*Hecht et al.*, 2008].

2. Data Set and Methods

[5] CRISM is a hyperspectral imaging spectrometer that covers 544 wavelengths between 0.364 and 3.936 μm at a spatial resolution of ~18 m/pixel in Full-Resolution Targeted (FRT) mode [*Murchie et al.*, 2007]. The detector is attached to a gimbal platform, which allows CRISM to acquire Emission Phase Functions (EPFs): multiple images of the same area taken from different angles as the spacecraft approaches, flies over, and moves away from the target. EPF sequences illustrate the effects of the atmosphere as well as scattering properties of the surface and aerosols.

[6] This study uses 25 CRISM FRT images taken directly over the landing site (on the ejecta deposit of the 10 km diameter Heimdal Crater) and 13 FRTs taken near the landing site, covering, for example, portions of Heimdal [*Arvidson et al.*, 2009]. Most of the FRTs were taken either directly over the landing site or over Heimdal Crater, covering the area from 68.117°N to 68.364°N and from 230.379°E to 235.701°E. The FRTs were taken at either 1500 or 0300 Local True Solar Time (LTST) (Figure 1). These data were acquired as part of a coordinated MRO-Phoenix observation campaign to map atmospheric and surface dynamics [*Tamppari et al.*, 2010]. FRT data utilized in this study were processed to units of *I*/*F* (radiance at the sensor divided by solar irradiance divided by pi). This study also uses ground observations from the SSI [*Smith et al.*, 2008], a stereo camera with 24 filters covering the spectral range of 0.445 to 1.001 μm.

2.1. Atmospheric Removal

[7] To remove atmospheric effects, gas and aerosol absorption and scattering, CRISM spectra were modeled with a Discrete Ordinate Radiative Transfer (DISORT) model [*Stamnes et al.*, 1988; *Wolff et al.*, 2007], which has been adapted for planetary applications ("DISORT_multi") [*Arvidson et al.*, 2005, 2006] and specifically for use with CRISM images [*Wiseman et al.*, 2009].

[8] DISORT calculates the *I*/*F* that CRISM would measure if looking through the atmosphere at a surface with known scattering properties. The atmosphere is treated as parallel layers of CO, CO_2, and H_2O gas, each with a specific pressure and temperature, and evenly distributed dust aerosols (ice aerosols are assumed to be well mixed above the point of water condensation) [*Wiseman et al.*, 2009]. The atmosphere over the Phoenix landing site at a given solar longitude is estimated from historical data from the Thermal Emission Spectrometer (TES): water column abundances are from *Smith* [2002], ice aerosols are estimated from TES optical depths at 12.1 μm [*Smith*, 2004], dust aerosols are estimated from CRISM EPF analysis at 0.9 μm [*Tamppari et al.*, 2010], surface pressure estimated from Viking 2 Lander results, and the atmospheric pressure profile calculated by integrating the hydrostatic equilibrium equation [*Conrath et al.*, 2000]. Dust aerosols are assumed to have a radius of 1.5 μm, a reasonable assumption given that the average non–dust storm dust aerosol is estimated to be between 1.2 and 1.8 μm [*Wolff et al.*, 2009]. Dust aerosol indicies of refraction and a wavelength-dependent phase function were derived from CRISM observations [*Wolff et al.*, 2009]. Water ice aerosols are assumed to have scattering properties from *Clancy et al.* [2003] and a radius of 2.0 μm, the median particle size observed by TES for ice aerosols in clouds [*Clancy et al.*, 2003].

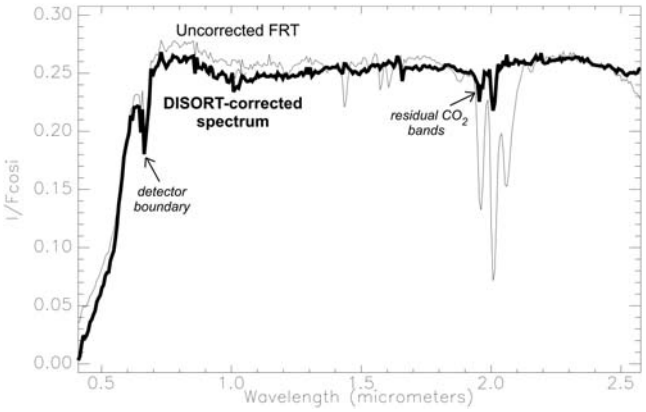

Figure 2. Uncorrected CRISM spectrum over Phoenix landing site (thin line) and DISORT-corrected spectrum (thick line). The sharp feature at ~0.65 μm is a detector boundary, and the two narrow features in the DISORT-corrected spectrum at 1.954 and 2.007 μm are residual CO_2 gas features.

[9] For DISORT calculations, the surface is assumed to scatter light according to a nonlinear mixing model based on [*Hapke*, 1981, 1993]

$$r(i,e,g) = \frac{w}{4\pi}\frac{\mu_0}{\mu_0+\mu}\{[1+B(g)]p(g)+H(\mu_0)H(\mu)-1\} \quad (1)$$

where i, e, and g are the incidence, emergence, and phase angles, respectively; $r(i, e, g,)$ is the bidirectional reflectance observed, μ_0 is the cosine of the incidence angle, μ is the cosine of the emergence angle, w is the single-scattering albedo, $B(g)$ is the opposition effect, $p(g)$ is the single-particle phase function, and $H(\mu_0)$ $H(\mu)$ describe multiple scattering. The opposition effect is ignored in this paper, because all of our observations were taken at phase angles >40°.

[10] The single-particle phase function is modeled with a two-lobed Henyey-Greenstein model [*Henyey and Greenstein*, 1941]:

$$p(g) = \frac{(1-\delta^2)f}{(1-2\delta\cos(g)+\delta^2)^{3/2}} + \frac{(1-\delta^2)(1-f)}{(1+2\delta\cos(g)+\delta^2)^{3/2}} \quad (2)$$

where f is a weighting factor that describes the scattering direction (f = 0 for forward scatter, f = 1 for backscatter), and δ is an asymmetry factor constrained to be between −1 and 1 (δ = 0 for isotropic scatter). The selection of $B(g)$, δ, and f parameters is discussed in section 2.4.

[11] CRISM center wavelengths shift slightly (<~1 nm) with instrument temperature changes [*Murchie et al.*, 2007]. To account for this, DISORT was run with 0.1 nm spacing over the CO_2 gas bands, and the wavelengths resampled and fit to the observed wavelengths to determine the offsets [*Wiseman et al.*, 2007]. The wavelength displacement is typically 0.3 to 0.7 nm for each wavelength.

[12] For each FRT, DISORT was run for surfaces with various w values: 0.25, 0.5, 0.7, 0.8, 0.9, and 0.99. The relationship between w and I/F for each band was modeled as a fifth-order polynomial, and a lookup table was generated to relate observed I/F to w. Equations (1) and (2) were then used to convert w to bidirectional reflectance. Atmospheric parameters were adjusted slightly to remove residual gas bands (or overcorrected gas bands), if needed (Figure 2). Typically, this adjustment consisted of small changes in ice or dust aerosols (tau ± 0.05) and was necessary for only a few FRTs considered in this study.

2.2. Modeling of Surface Spectra

[13] This study addresses two surface components: water ice and soil. Ice-free surfaces at the Phoenix landing site have relatively featureless spectra between 1.0 and 2.7 μm, but are highly absorbing at wavelengths <1.0 μm (Figure 3a). Water ice, on the other hand, is translucent at short wavelengths, but has strong absorptions at 1.5 and 2.0 μm and dramatically changes the shape of the spectrum between 2.3

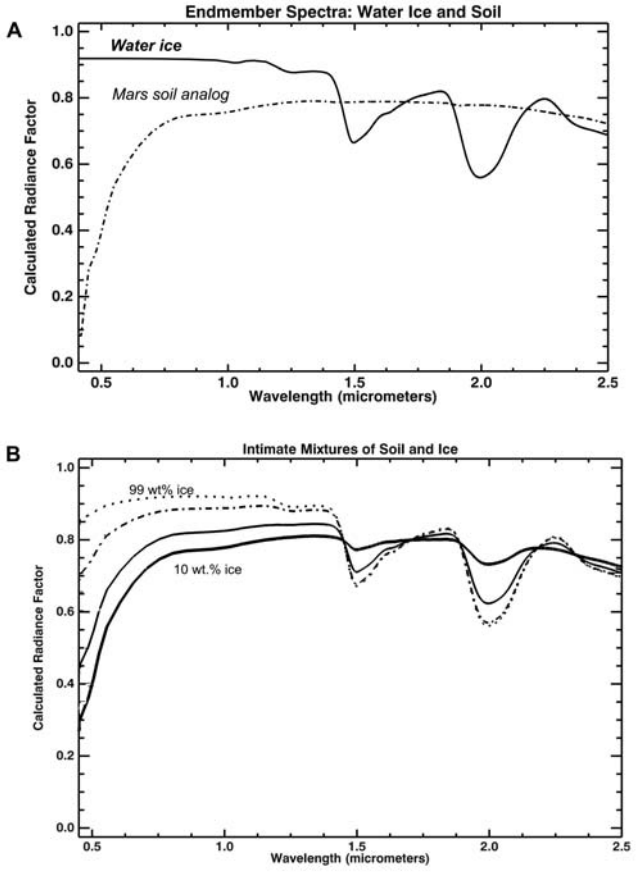

Figure 3. (a) Example spectra for 10 μm water ice (solid line) and 5 μm Mars soil analog (dotted line). Water ice is featureless at shorter wavelengths and has strong absorptions at 1.5 μm, 2.0 μm, and a distinctive negative slope between 2.3 and 2.6 μm. Soil is featureless at longer wavelengths but has a sharp "red edge" at short wavelengths. (b) Examples of intimate mixtures of soil and ice with various mass ratios: 10 wt % ice (heavy line), 50 wt % ice (thin line), 90 wt % ice (dashed-dotted line), and 99 wt % ice (dotted line). Dust mass fractions greater than ~90 wt % will mask water ice absorptions; however, >99 wt % ice is needed to completely mask the ferric red edge. In these examples, we

and 2.6 μm due to a strong 3.17 μm absorption (Figure 3a). For mixtures or layers of water and ice, light interacts with both components before reaching the detector, so the shape and albedo of the final spectrum is a nonlinear mixture of the two components (Figure 3b).

[14] CRISM bidirectional surface reflectance spectra were extracted from the Heimdal Outer Ejecta unit (lowland bright unit of *Seelos et al.* [2008]) on which Phoenix landed [*Heet et al.*, 2009] and is widespread around the Phoenix landing site. Five-by-five pixel average spectra were compared across the unit in each scene and a representative spectrum selected for modeling. For observations taken over the landing site, spectra were selected from near the landing site itself. Spectra were extracted only from central areas of each image to avoid effects of spectral smile [*Murchie et al.*, 2007].

[15] To extract grain sizes and relative abundances from CRISM observations, each spectrum was simulated using the nonlinear mixing model based on equations (1) and (2) [*Hapke,* 1981], and a two-layer model described in equations (9.31a)–(9.31e) of *Hapke* [1993]. Single-scattering albedos of component mixtures were calculated as

$$w = \frac{\sum_{i=1}^{i=n}(Q_{Si}M_i/\rho_i D_i)}{\sum_{i=1}^{i=n}(Q_{Ei}M_i/\rho_i D_i)} \quad (3)$$

where M_i is the mass fraction of component i, ρ_i its solid density, D_i its diameter, Q_{Si} the scattering efficiency, Q_{Ei} the extinction efficiency, and the summation is carried out for all components in the n component mixture. Scattering efficiency was calculated as described by *Roush* [1994], and extinction efficiency was set to 1, because the particles being considered are large compared to the wavelength and so are affecting the entire wavefront [*Hapke*, 1981].

[16] As described above, this model depends on viewing geometry, grain complex indicies of refractions, sizes, solid densities, relative mass fractions of each component; and the surface porosity and scattering parameters: δ and f. Water ice optical constants were used from *Warren* [1984]. Soil optical constants were from *Clancy et al.* [1995], which are derived from Mauna Kea palagonite, a low-temperature alteration product of fine-grained basaltic ash. The Mauna Kea palagonite appears to be a good analog for the Phoenix site soils [*Heet et al.*, 2009], although it has a slightly shallower slope between 0.7 and 1.0 μm. A solid density of $\rho = 0.9167$ g/cm^3 was used for water ice, and $\rho = 2.700$ g/cm^3 for soil. We assume a surface porosity of 50%, similar to the Viking 2 landing site [*Moore et al.*, 1987], because Phoenix soil physical properties appear similar to the Viking 2 landing site in general [*Arvidson et al.*, 2009]. The 50% porosity is also supported by modeling of Phoenix soil thermal inertia based on data from the Thermal and Electrical Conductivity Probe (TECP) (A. Zent, personal communication, 2008). For ice layers, we assume a porosity of 70%, similar to a typical winter snowpack on Earth; however, we find that, for very thin layers (<1 mm), top layer porosity does not affect results for porosities between ~40 and ~80%. For each CRISM spectrum, we use the same scattering parameters used in DISORT modeling of that spectrum. Scattering parameter constraints are described in section 2.4.

[17] In the layered models, the thickness of the overlying layer was calculated based on the cross-sectional mass (e.g., mg/cm^2). To convert this to a layer thickness, the cross-sectional mass was divided by the material's solid density.

[18] With these assumptions, the grain sizes and relative mass fractions of the two components were varied to match each CRISM spectrum.

2.3. Sensitivity Analysis

[19] Because Hapke modeling can produce nonunique results (for example, trading grain size for mass fraction can produce similar spectra), a sensitivity analysis was used to test the uniqueness of each result. First, a set of best fit parameters was found by inspection and a chi-squared (X^2) value calculated:

$$\chi^2 = \sum_{\lambda=1}^{n} \frac{(r_o - r_m)^2}{r_o^2} \quad (4)$$

where r_o is the observed bidirectional reflectance, r_m is the modeled bidirectional reflectance, and the summation is carried out over all wavelengths (except between 1.95 μm and 2.1 μm, an area sometimes disrupted by residual CO_2 gas bands in DISORT-derived spectra).

[20] This initial set of parameters represented a local minimum in X^2 space. To test for other local minima, one parameter (grain size, mass ratio, or upper layer thickness) was stepped away from the initial value while the other parameters were allowed to vary and new X^2 values calculated. In this way, for each spectrum, one to three local minima were identified. Some of these could be discarded as actual best fit solutions either because their absorption band depths did not match the band depths of the CRISM spectrum, or because they were physically unreasonable (for example, 30 μm grains in a layer of material only 15 μm thick). After discarding unreasonable local minima, if the FRT still had more than one local minimum, then the FRT was discarded as being too poorly constrained.

[21] Once a single best fit local minimum was found, we tested how well constrained were each of the variables within that solution by systematically varying one parameter and recalculating X^2 values. If the parameter was well constrained, the X^2 value should increase quickly as it is varied (e.g., Figure 8c). If the parameter is poorly constrained, it should increase slowly away from the best fit value (e.g., Figure 8b).

2.4. Constraining Surface Scattering Parameters

[22] DISORT-based single-scattering albedo retrievals and nonlinear mixing model results are sensitive to the surface phase function parameters (δ and f), and the magnitude (B_0) and width (h) of the opposition effect (the latter two are ignored, as discussed above). Deriving these parameters for the Phoenix landing site is beyond the scope of this paper; however, the parameters selected must approximate the behavior of the Phoenix surface for the DISORT and Hapke modeling to be effective.

[23] *Johnson et al.* [2006] used Spirit Rover data to derive scattering parameters for various materials at Gusev Crater. To approximate the Phoenix landing site, DISORT was used to model surfaces with Gusev scattering parameters over a range of viewing geometries. The resulting relationships between radiance and viewing geometry were compared to the CRISM EPFs, and the closest-fitting set of scattering

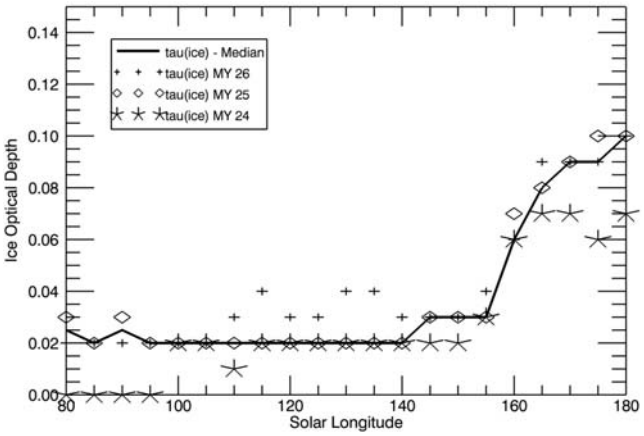

Figure 4. Historical ice aerosol optical depths as observed by TES for Mars Year (MY) 24, 25, and 26.

parameters selected. Spectra for the EPF sequences were selected by averaging the central 20 pixels of each line within the EPF.

2.5. Separating Ice Aerosols From Surface Ice

[24] Water ice produces major absorptions at 1.52, 1.94, 2.02, 2.96, and 3.17 μm [*Gaffey et al.*, 1997], regardless of whether it is on the surface or in the atmosphere. Although the DISORT modeling removes contributions from ice aerosols, the initial inputs are based on historical ice optical depths, which vary slightly from year to year (Figure 4). An incomplete removal of ice aerosol signatures could result in a positive identification for surface ice, when in fact the ice bands are due to ice aerosols.

[25] To assess whether water ice bands are due to surface ice, ice aerosols, or a combination of the two, the relative band depths of the 1.5 μm and 3.17 μm bands were compared for each scene. Band depths were calculated as defined by *Pelkey et al.* [2007]:

$$BD = 1 - \frac{R(\lambda_C)}{aR(\lambda_S) + bR(\lambda_L)} \quad (5)$$

where $R(\lambda)$ is the reflectance measured at wavelength λ, λ_C is the center wavelength for the band depth being measured, the continuum is defined between wavelengths λ_S and λ_L, $b = (\lambda_C - \lambda_S)/(\lambda_L - \lambda_S)$, and $a = 1 - b$. For the 1.5 μm band depth, $\lambda_C = 1.510$ μm, $\lambda_S = 1.330$ μm, and $\lambda_L = 1.695$ μm. For the 3.17 μm band depth, $\lambda_C = 3.170$ μm, $\lambda_S = 2.22$ μm, $\lambda_L = 3.72$ μm.

[26] The 3.17 μm band is more sensitive to the presence of water ice than the 1.5 μm band, as noted in OMEGA data by *Langevin et al.* [2007]. This is because the 3.17 μm feature is due to the fundamental ν_1 vibration and is approximately an order of magnitude stronger than the 1.5 μm, which is due to the $2\nu_3$ overtone. The 3.17 μm band appears for very small water ice grain sizes or abundances, and, with increasing grain size, saturates quickly. The 1.5 μm band appears for larger grain sizes and abundances and deepens more slowly with increasing grain size. The ratio between the 3.17 μm band depth and the 1.5 μm band depth, then, is high for small grain sizes or abundances, and smaller for large grain sizes or abundances.

[27] To illustrate the relationship between surface ice grain size and the 3.17 to 1.5 μm band depth ratio, bidirectional reflectances were calculated for icy surfaces with varying ice grain sizes, using the model described in section 2.2. To illustrate the relationship between atmospheric ice and the 3.17 to 1.5 μm band depth ratio, DISORT models were run with varying ice optical depths (0.0, 0.01, 0.02, 0.04, 0.05, 0.06, 0.07, 0.08, 0.09, 0.1, 0.15). Results from these runs are presented in section 3.2.

[28] To distinguish between surface and atmospheric ice in the CRISM observations, the 1.5 μm and 3.17 μm band depths were calculated for the atmospherically uncorrected observations. For each, the 3.17/1.5 μm band depth ratio was compared to those for surface and atmospheric ices. Results from these analyses are presented in section 3.2.

3. Results

3.1. Constraining Scattering Parameters

[29] An example of an ice-free CRISM EPF sequence over Phoenix is shown in Figure 5 for FRT0000B1D2 at

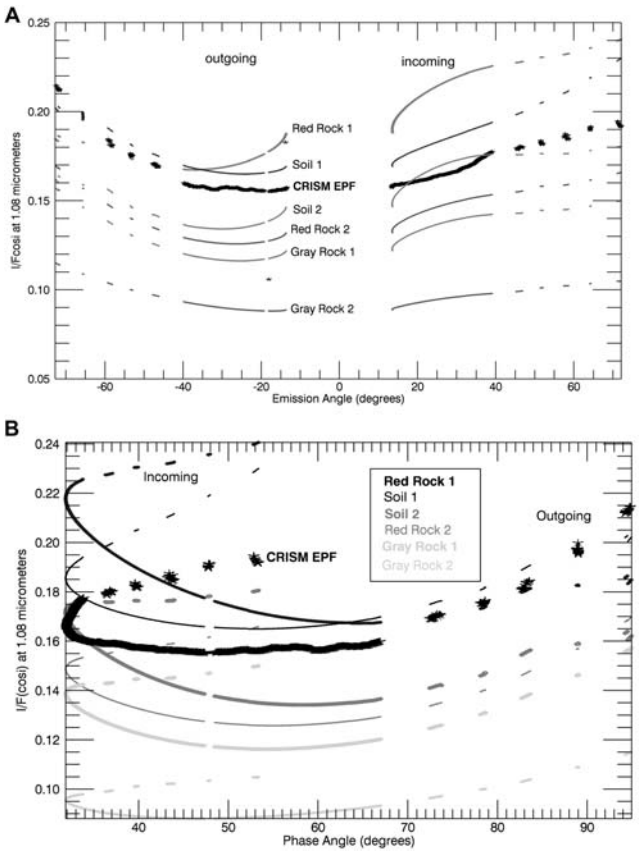

Figure 5. DISORT models (gray lines) simulating FRT0000B1D2 (black line) over the Phoenix landing site for various (a) emergence and (b) phase angles. Each gray line represents a Hapke surface with scattering parameters (w, δ, f, B_0, h) from one of the Gusev Crater materials described by *Johnson et al.* [2006]. The surfaces were overlaid with a model atmosphere based on FRT0000B1D2, and the viewing geometry varied to observe the effects on radiance. The emergence angle gap between −13° and 13° is due to the spacecraft roll angle during acquisition.

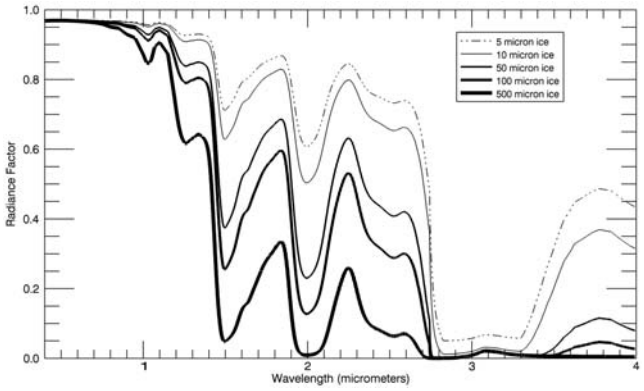

Figure 6. Models of surface ice of various grain sizes, showing the effects of surface ice grain size on the 3.17/1.5 μm band depth ratio. The 3.17 μm water ice band saturates for even small grain sizes, resulting in a small 3.17/1.5 μm band depth ratio. For larger grain sizes, as the 1.5 μm band nears saturation, the 3.17/1.5 μm band depth ratio approaches 1.

1.08 μm. The EPFs are poorly approximated by a Lambertian surface, which produces a scattered radiance that is independent of emergence or phase angles. They are also poorly approximated by scattering properties similar to the gray rock or red rock end-members described by *Johnson et al.* [2006]. The Phoenix EPFs are closer to the soil end-members derived by *Johnson et al.* [2006] for the Spirit landing site at Gusev Crater: an asymmetry parameter of 0.498, forward-scattering fraction of 0.817, B_0 of 1, and h of 0.385. The Gusev Crater Soil end-member is a widespread plains unit that is photometrically to similar to many Martian soils, including dusty surfaces at the Viking 1 landing site [*Arvidson et al.*, 1989] and soils at the Mars Pathfinder landing site [*Johnson et al.*, 1999].

3.2. Atmospheric Versus Surface Ice

[30] The 3.17 to 1.5 μm band depth ratio described in section 2.5 were used to distinguish between atmospheric and surface ices. For surface ice (Figure 6), the ratio decreases with increasing grain sizes; however, the ratio is always relatively small: in the 1 to 8 range. Ice aerosols (Figure 7) follow a similar pattern: higher 3.17/1.5 ratio for lower ice optical depths. For example, an ice optical depth of 0.05 produced a 3.17/1.5 ratio of 234, while an optical depth of 0.1 produced a ratio of 109. Although the ratio becomes smaller for high ice optical depths, it is always much higher than for surface ice: between 100 and 500. The 3.17/1.5 ratio is so much lower for surface ices because, due to their higher concentration and larger grain sizes, the 3.17 μm band is saturated; the more surface ice, the deeper the 1.5 μm band, and the lower the 3.17/1.5 ratio. Ice aerosols, on the other hand, are not densely packed enough to saturate the 3.17 μm band and have only a minor impact on the 1.5 μm band.

[31] The 3.17/1.5 ratio, then, can be used to distinguish between ice signatures due to surface ice, atmospheric ice, or a combination of the two. High 3.17/1.5 ratios (>50) are taken to indicate that most of the ice band contributions are from ice aerosols. Low 3.17/1.5 ratios (<10) are taken to indicate mostly surface contributions. Intermediate 3.17/1.5 ratios (10–50) are taken to indicate a combination of surface and atmospheric ice contributions.

[32] Water molecules adsorbed onto the surface also produce an absorption at 3.05 μm, which, when strong enough, could affect the spectrum at 3.17 μm. Adsorbed water does not produce a 1.5 μm absorption (its $2\nu_3$ overtone appears at 1.45 μm) [*Gaffey et al.*, 1997], so its presence could affect the 3.17/1.5 μm ratios. However, because the 3.17 μm band is already saturated in all of the icy FRTs considered here, adsorbed water does not influence the 3.17/1.5 μm ratio.

[33] To test the validity of the 3.17/1.5 μm ratio method for distinguishing ice aerosols from surface ice, we performed the same analysis on three CRISM cubes: an early spring (L_s ~ 34°) observation known to have significant amounts of surface ice [*Cull et al.*, 2010], a midspring (L_s ~ 42°) observation with small amounts of surface ice, and a late spring (L_s ~ 68°) observation with no surface ice at all. These observations have comparable ice aerosol optical depths (~0.03 from historical TES data). The early spring observation was found to have a 3.17/1.5 μm ratio of 2.9, midspring a ratio of 13.25, and late spring a ratio of 255.0.

3.3. Late Spring to Early Summer

3.3.1. Ice-Free Spectrum

[34] The last of the seasonal cap water ice disappears from the Phoenix landing site by L_s ~ 59° [*Cull et al.*, 2010]. Between L_s ~ 59° and L_s ~ 104°, 13 FRTs were acquired; these show an ice-free surface. Hapke modeling of three observations produced a best fit using two layers of soil: a fine-grained (15 μm) layer (~100 μm thick) on top of a layer of sand-sized (2 mm) soil particles (analysis of FRT0000B1D2 is shown in Figure 8a). A sensitivity analysis conducted on these models shows that the size of the

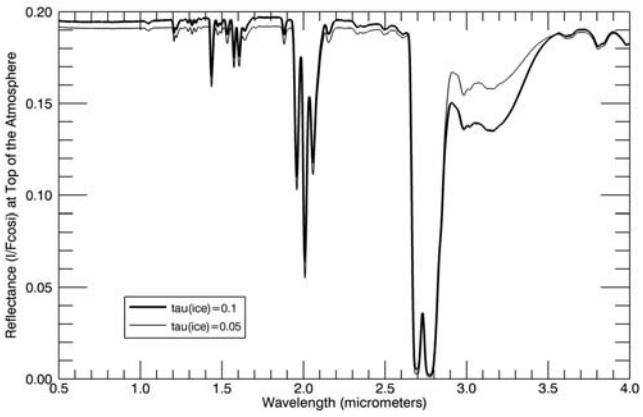

Figure 7. Atmospheric spectra with various ice opacities showing the effect of ice opacity on the 3.17/1.5 μm band depth ratio. The 1.5 μm absorption is shallow for all opacities; whereas, the 3.17 μm absorption deepens significantly with increasing opacity. The result is a high 3.17/1.5 μm band depth ratio that only falls below 100 for ice opacities greater than ~0.1. Ice opacities are relative to 12.1 μm.

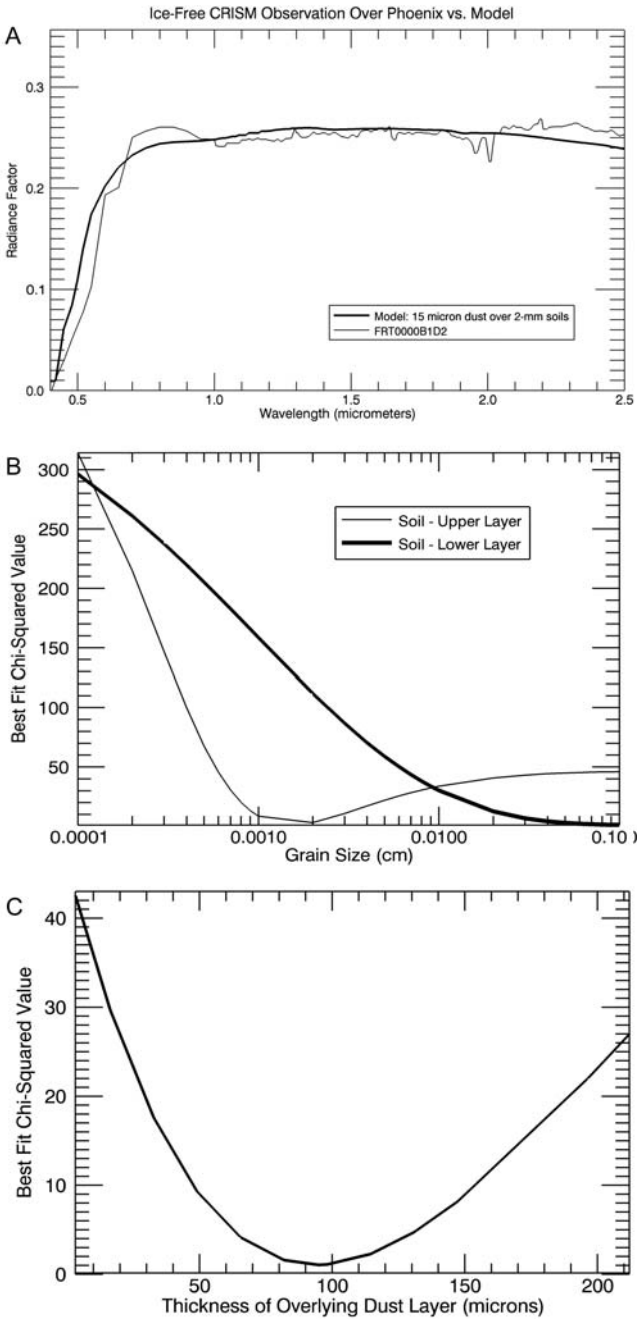

Figure 8. (a) Ice-free summer spectrum over the Phoenix landing site (FRT0000B1D2, thin line), and model results (thick line). The spectrum is best modeled by a ~100 μm thick layer of silt-sized particles (~15 μm) overlying sand-sized particles (~2 mm). Sensitivity analysis for (b) grain sizes and (c) thickness of dust layer.

sand-sized particles is poorly constrained on the upper end (Figure 8b); however, the dust grain size is constrained to be between ~10 and 30 μm, with a clear minimum at 15 μm. This combination was seen consistently for ice-free observations over multiple L_s and multiple observations, including ice-free observations reported by *Cull et al.* [2010].

3.3.2. Permanent and Mobile Summer Ices

[35] Although the surface in general is ice-free during the late spring and early summer, several patches of permanent ice were observed. *Seelos et al.* [2008] reported permanent patches of summertime ices on the north facing wall of

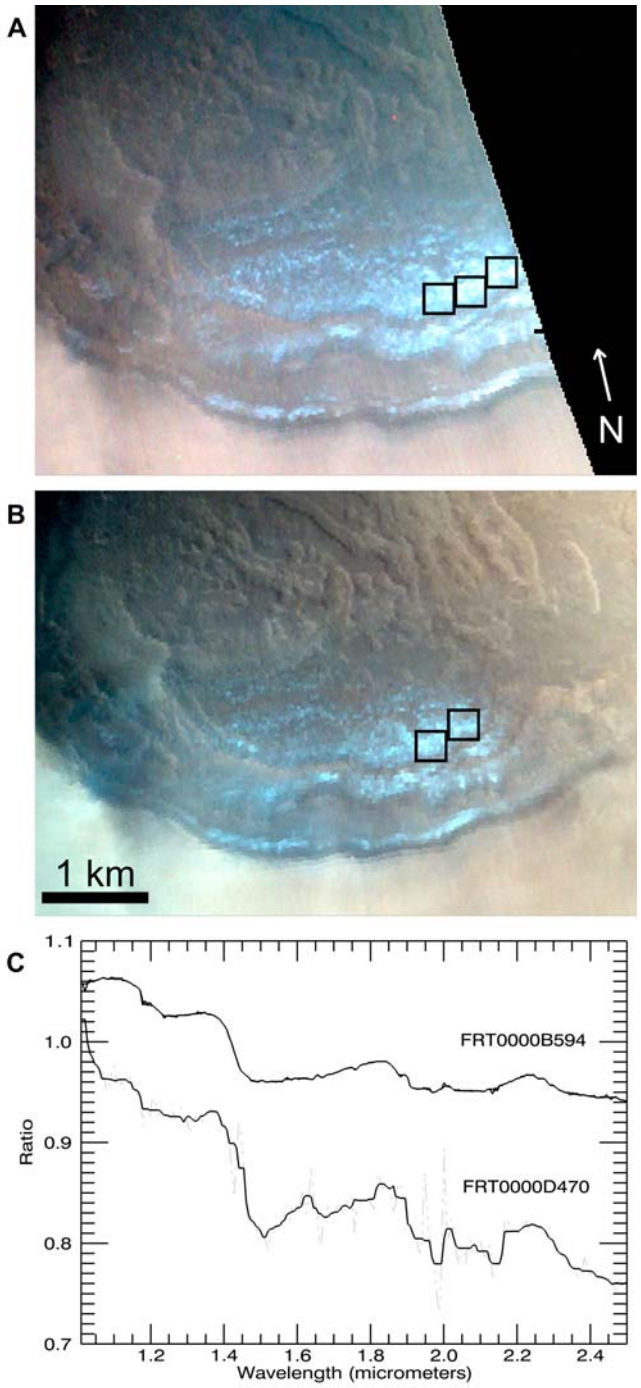

Figure 9. Permanent water ice deposits on the north facing slopes of Heimdal Crater. (a) FRT0000B594, L_s ~ 94°. (b) FRT0000D470, L_s ~ 154°. (c) Ratio spectra of icy patches to non–icy patches (dotted gray lines) and with a median filter applied (solid lines). The absorptions at 1.5 and 2.0 μm are due to water ice.

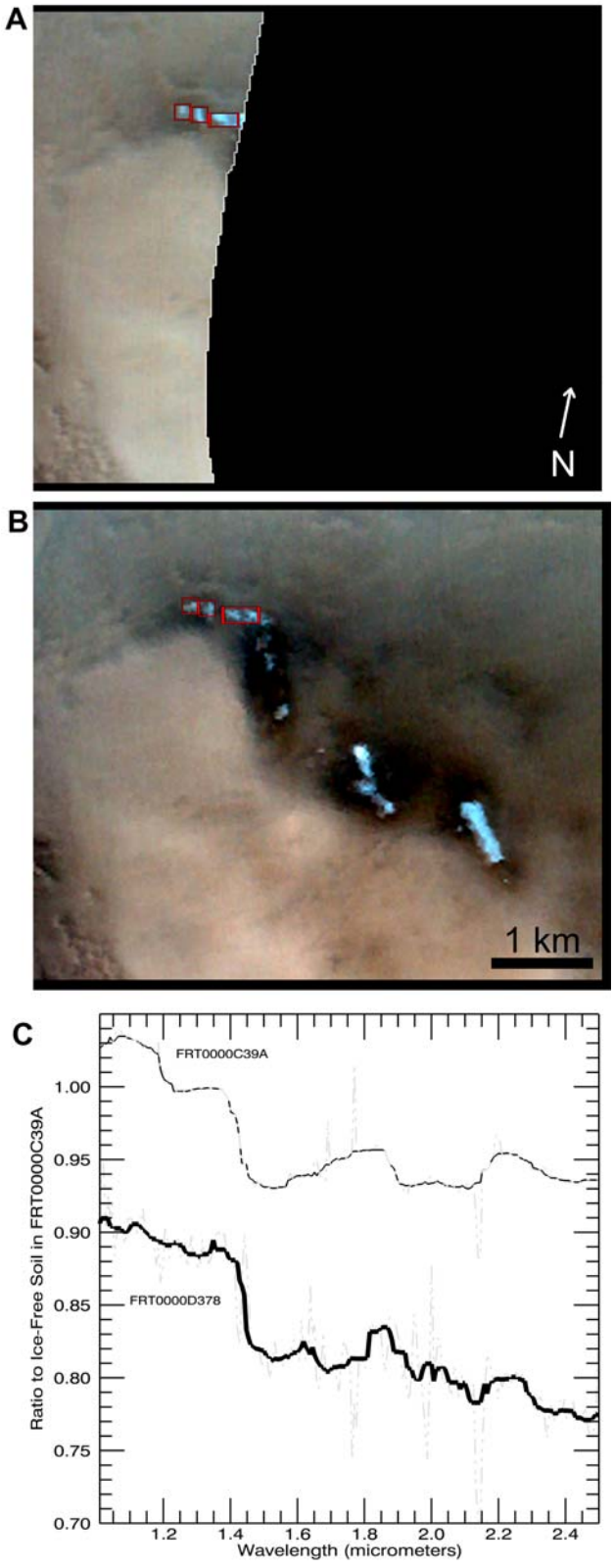

Figure 10. Permanent water ice deposits on the north facing slopes of a plateau northeast of Heimdal Crater. (a) FRT0000C39A, L_s ~ 119°. (b) FRT0000D378, L_s ~ 151°. (c) Ratio spectra of icy patches to non–icy patches (dotted gray lines) and with a median filter applied (solid lines). The absorptions at 1.5 and 2.0 μm are due to water ice.

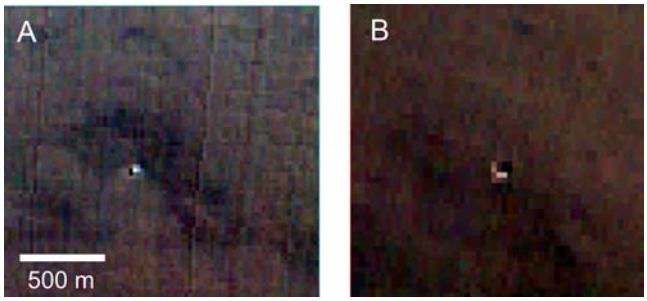

Figure 11. Water ice in 85 m crater northeast of the Phoenix landing site. (a) FRT0000B1D2, L_s ~ 86°, 1300 LTST. (b) FRT0000B079, L_s ~ 84°, 0300 LTST. In the nighttime image, the ice has moved from one crater wall to the opposite, avoiding the sunlight.

Heimdal Crater (Figure 9) and the northern slopes of ejecta deposits to the northeast of Heimdal (Figure 10), similar to the permanent patches of water ice observed on the walls of Louth Crater by *Brown et al.* [2008]. These ices were monitored throughout the summer as part of the CRISM-Phoenix coordinated observation campaign.

[36] The water ice patches, both on the north facing wall of Heimdal and on the north facing slopes of the mountains to the northeast, do not appear to grow or shrink during the summer (Figures 9 and 10). However, for both ice patches, the overall albedo darkens from early to late summer (L_s ~ 94° to ~160°), and the water ice band depths deepen from ~3% at L_s ~ 119° to ~6% at L_s ~ 160° (Figures 9 and 10), implying that the water ice is becoming coarser grained. It is possible that fine-grained water ice is cold trapped onto the ice patches during the spring defrost period, when water ice is sublimating from the surrounding terrain and filling the atmosphere with water vapor. The fine-grained surface ice could then either sinter into coarser grains, a relatively

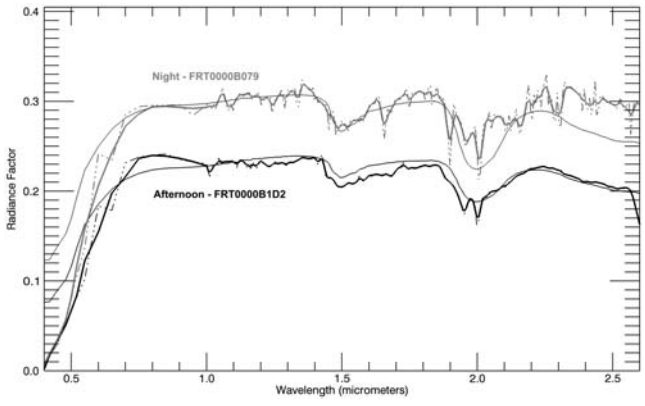

Figure 12. CRISM spectra of ice (thick lines) in the 85 m crater at 1300 LTST(black) and 0300 LTST (gray) with model results (thin lines) for each. The afternoon observation is modeled as ~150 μm thick layer of 50 μm ice overlying a typical ice-free mixture (silt- and sand-sized particles). The nighttime observation is best modeled as a slightly thicker (~165 μm) layer of 50 μm ice over the same mixture.

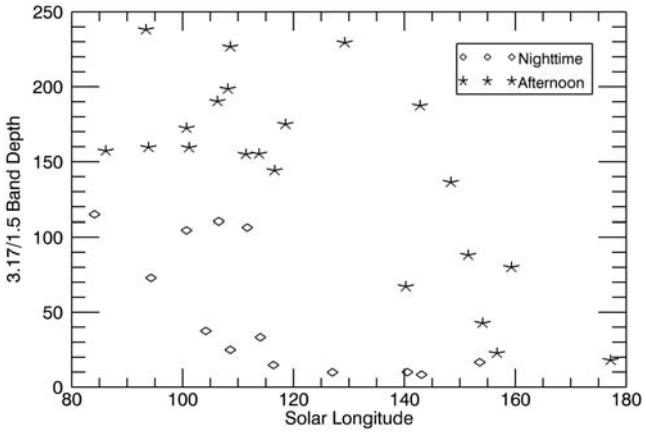

Figure 13. The ratios of the 3.17 to 1.5 μm band depths for CRISM observations over the Phoenix landing site through time. In the late spring and early summer the ratios are higher, indicating small ice optical depths and no surface ice. The nighttime ratios drop quickly starting at $L_s \sim 104°$, indicating a growing contribution from surface ice. The afternoon ratios begin dropping around $L_s \sim 155°$.

common and rapid processes for polar ices [*Eluszkiewicz*, 1993], or sublimate as atmospheric temperatures continue to rise during midsummer and late summer, exposing the coarser-grained permanent ice.

[37] In addition to the patches of permanent ice, mobile patches of summertime ices were observed. At 1500 LTST at $L_s \sim 86°$, water ice was observed on the shadowed wall of an ~85 m crater located ~6.5 km northeast the landing site (68.29°N, 234.46°W; Figure 11). A 0300 LTST CRISM observation of the same crater, taken four sols earlier, shows the ice on the opposite crater wall. The ices in both these images are best modeled as fine-grained (~50 μm) water ice overlying a silt-sand mixture (Figure 12), presumably cold trapped onto the soil. The nighttime observation is significantly brighter than the daytime observation, perhaps due to a combination of a slightly thicker ice deposit (~165 μm versus ~150 μm), a higher ice:dust ratio (40% ice versus 30% ice), or different viewing geometry (g = 83.1, i = 77.4 versus g = 38.6, i = 52.8).

3.3.3. Nighttime: Surface Frost and Atmospheric Ice

[38] Sixteen nighttime observations (0300 LTST) were made over the Phoenix landing site between $L_s \sim 84°$ and

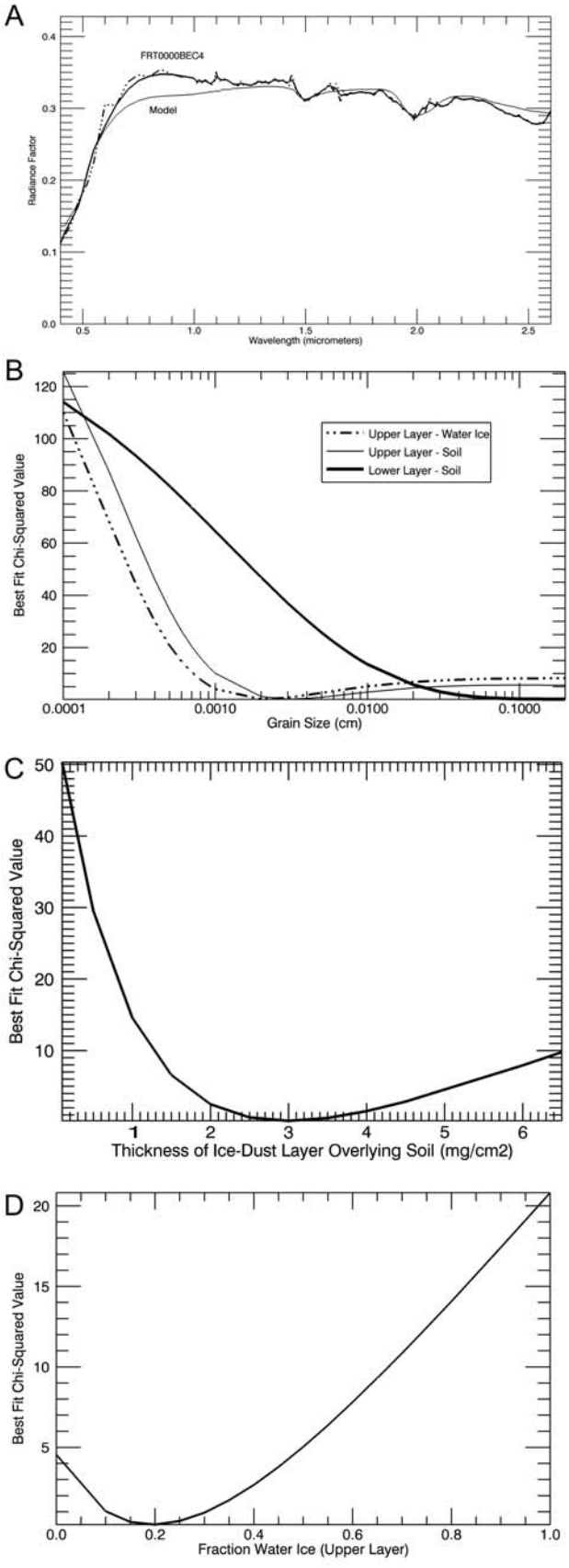

Figure 14. (a) Nighttime spectrum over the Phoenix landing site (FRT0000BEC4, thick line), and model results (thin line): a thin (~115 μm) layer of water ice (20 μm) and dust (30 μm) overlying sand-sized (2 mm) soil (X^2 = 0.1968). The absorptions at 1.5 and 2.0 μm are due to water ice. (b) Sensitivity analysis on this model illustrates that (with all other parameters set to the above values) the grain sizes are well constrained at the lower end, but poorly constrained on the higher ends. The grain sizes of the lower layer of soil are particularly poorly constrained on the high end, being best fit for grain sizes >1 mm. (c) The thickness of the overlying soil and (d) the fraction of water ice in the overlying layer are well constrained.

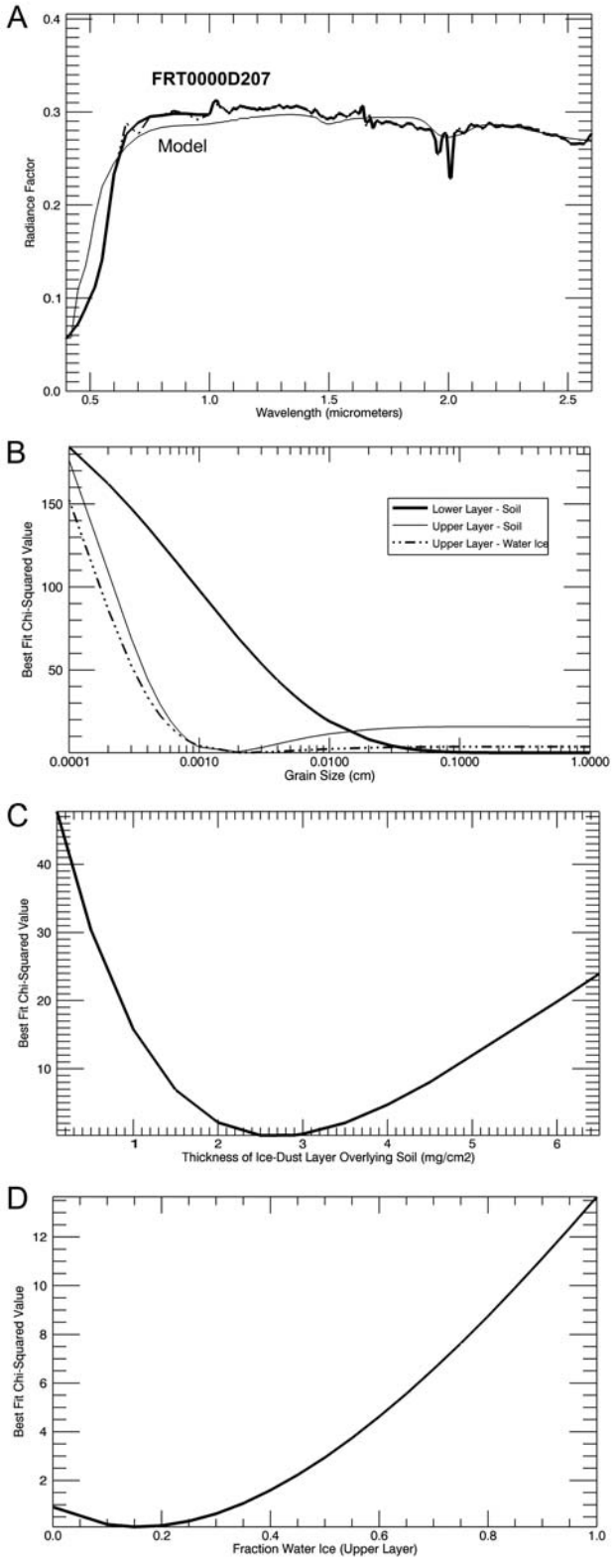

Figure 15. Afternoon surface frost at the Phoenix landing site (thick line, FRT0000D207) versus model result (thin line): a thin layer (~100 μm) of ~15% 20 μm water ice with ~85% 15 μm dust overlying sand-sized (2 mm) soil particles (X^2 = 0.089). Sensitivity analyses were performed with all parameters set to these values, and only the parameter of interest allowed to vary.

L_s ~ 154°. Prior to L_s ~ 114°, the nighttime observations have high 3.17/1.5 band depth ratios (median ~104), indicating a high ice aerosol optical depth (>0.08; Figure 13). Two observations (L_s ~ 104° and 109°, sols 61 and 70) have 3.17/1.5 ratios less than 50, indicating either exceptionally high ice optical depth, or a significant contribution from surface ice.

[39] The nighttime water ice spectrum is best fit by a thin layer (~115 μm) of ~30% 20 μm water ice with ~70% 30 μm dust overlying sand-sized (2 mm) soil particles (X^2 = 0.197) (Figure 14a). Alternative layer configurations (e.g., ice over icy dust, a single layer of icy dust, etc.) did not fit

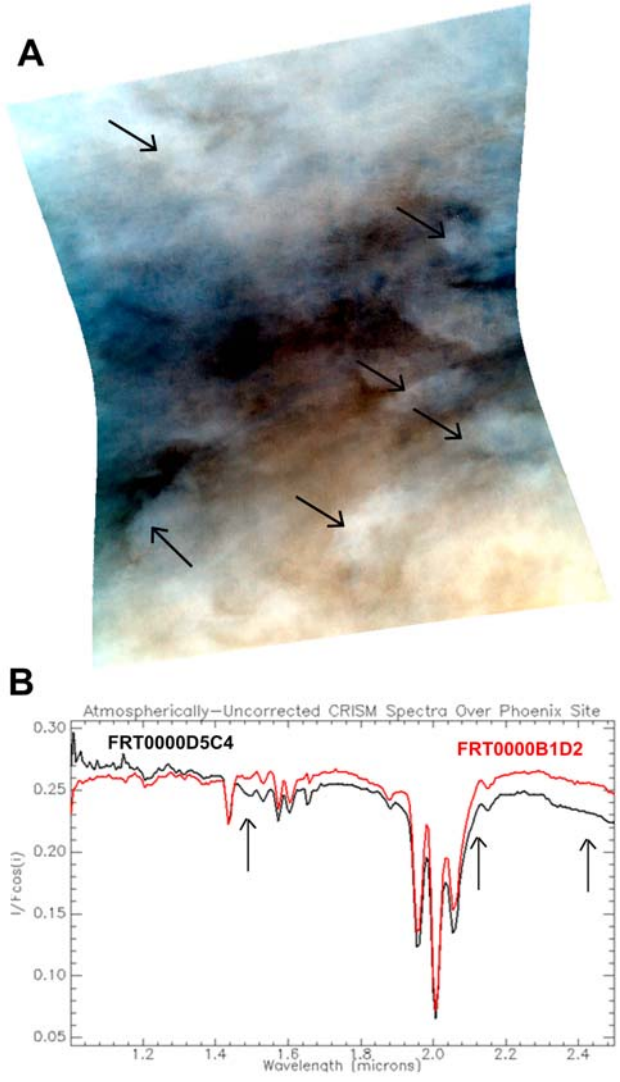

Figure 16. (a) False color CRISM observation of afternoon clouds over the Phoenix landing site (FRT0000D5C4; R, 0.7097 μm; G, 0.5989 μm; B, 0.5337 μm). (b) Cloudy spectrum (black, an average of the areas marked by the black arrows above) compared to a spectrum with low ice aerosols (FRT0000B1D2, red). The cloudy observation has a clear water ice absorption at 1.5 μm, and the shape of the spectrum has changed significantly at 2.0 μm and between 2.3 and 2.5 μm.

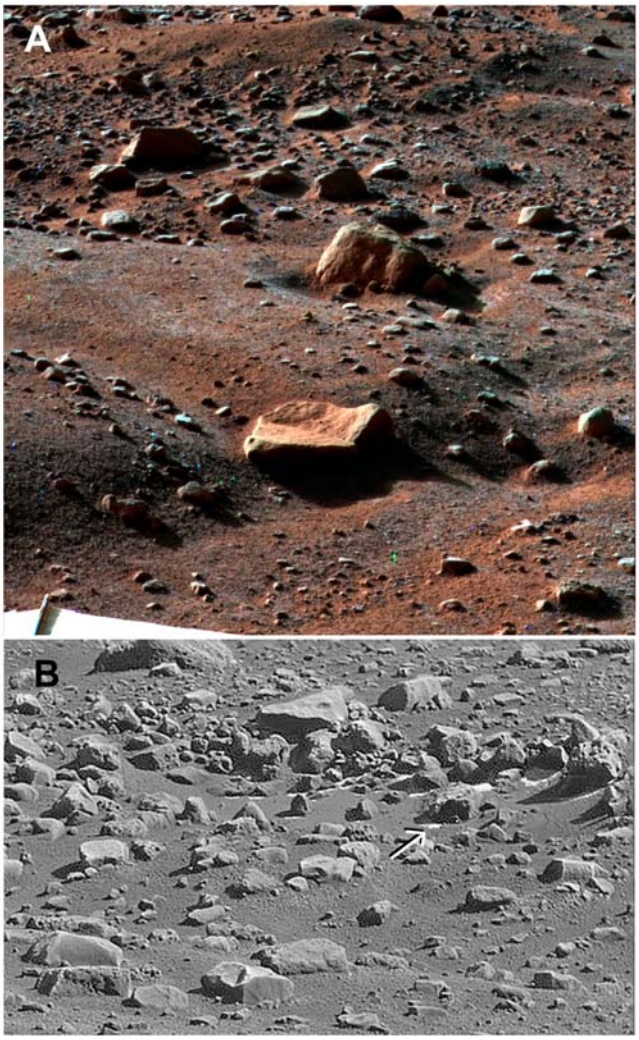

Figure 17. (a) SSI false color (R, 0.75 μm; G, 0.53 μm; B, 0.44 μm) composite of "Winkies" (an ~27 cm rock in the foreground) on sol 79 at ~0600 LTST. White-blue frost is visible on the soil behind Winkies. (b) Ratio of SSI filters L2 to LC (0.445 μm to 0.967 μm) for "Jumping Cow" area on sol 80 at ~1300 LTST. The white patches on the shadowed sides of the rocks are interpreted to be water ice.

the observed spectrum. The grain sizes for the overlying layer are well constrained for both the ice and the soil; however, the underlying soil grain size is poorly constrained, except to say it must be sand sized (>1 mm; Figure 14b). The thickness of the overlying ice-soil layer and the fraction of water ice in the upper layer are both well constrained.

3.3.4. Afternoon: Surface Frost and Atmospheric Ice

[40] Similar to the nighttime ice pattern, afternoon ice absorptions are dominated by ice aerosols (3.17/1.5 ratios >50) until L_s ~ 154°, after which there are only five observations. The 3.17/1.5 ratios tend to be higher for afternoon surface ice absorptions, probably because the daytime ice optical depths are lower than those for the nighttime. Surface ice is dominating water ice absorptions after L_s ~ 154° (Figure 13): the 3.17/1.5 band depth ratios of ~10 to ~30 over non-cloud-covered areas indicate a contribution from both surface ice and atmospheric ice. The surface ice is best modeled as a thin layer (~100 μm) of ~15% 20 μm water ice with ~85% 15 μm dust overlying sand-sized (2 mm) soil particles (X^2 = 0.089) (Figure 15a). As with previous observations, the sand size is poorly constrained (Figure 15b), while the other variables are better constrained (Figures 15c and 15d).

[41] Afternoon water ice clouds were observed in CRISM images starting at L_s ~ 157° (Figure 16). The clouds appeared as distinct hazes in the FRT and had obvious 1.5 and 3.17 μm water ice absorptions, with 3.17/1.5 band depth ratios of ~50 to 165, indicating a combination of surface ice and atmospheric ice. Phoenix's lidar instrument did not detect afternoon clouds during surface operations, which ended at L_s ~ 149° [*Whiteway et al.*, 2009].

4. Discussion

4.1. Ice-Free Soils

[42] CRISM spectra over the Phoenix landing site are consistently best fit only by including a sand-sized (2 mm) component to the lower layer of soil (adding it to the upper layer darkens the spectrum more than is observed). Phoenix's OM experiment measured a mean grain size of ~90 μm by mass (T. Pike, personal communication, 2008). However, the OM experiment is biased toward smaller grain sizes, because samples were first delivered to the imaging substrate, then rotated 90 degrees prior to imaging, and, as a result of tilting, larger particles may have fallen off. Additionally, Phoenix observations indicate that the soil was highly cohesive and large aggregates of small particles were commonly observed [*Arvidson et al.*, 2009]. RAC images of soil attached to the "divot" of the Icy Soil Acquisition Device (ISAD) [*Bonitz et al.*, 2008] routinely show aggregates of soil on the order of 5 mm (in for example, RAC images RS 072 EFF 902585678_18230MB M1 and RS 099 FFL 904986760_1B7F0MR M1). We therefore conclude that the 2 mm "grains" needed for modeling these spectra are in fact aggregates of small particles that behave like larger grains.

[43] Ice-free spectra have a slight negative slope between 2.3 and 2.6 μm, caused by the strong water absorption near 3 μm, indicating a low level of hydration or adsorption of water, an effect seen throughout the northern hemisphere in both CRISM and OMEGA data [*Jouglet et al.*, 2007; *Poulet et al.*, 2008]. *Milliken et al.* [2007] speculated that this was due to hydrated minerals, which contributed ~10 wt % water to the surface. However, the lack of a 1.9 μm absorption argues against the water feature being due to hydrated mineral phases. Additionally, surface samples analyzed by the Thermal Evolved Gas Analyzer (TEGA) contained less than ~1 wt % water [*Smith et al.*, 2009]. *Arvidson et al.* [2009] proposes that the 1.9 and 3 μm bands are more likely due to thin layers of water molecules adsorbed onto the surface.

4.2. Appearance of Surface Ice

[44] This study first observed nighttime water ice on the surface around L_s ~ 109°, corresponding to sol 70 of Phoenix operations. Although MARCI images taken during the L_s ~ 109° observation show bright water ice clouds west

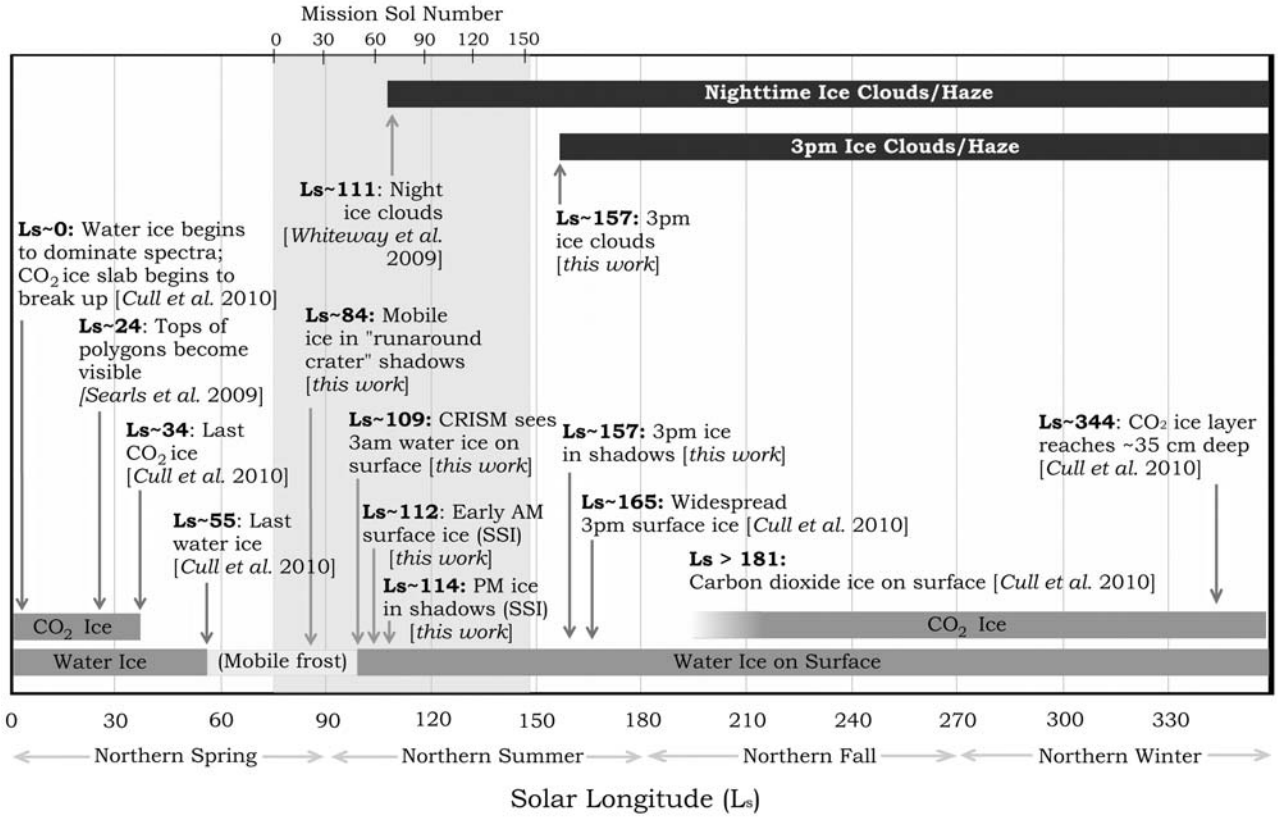

Figure 18. The seasonal ice cycle at the Phoenix landing site.

of the landing site, SSI imaging at 0700 LTST on the morning of sol 71 show no water ice aerosols [*Tamppari et al.*, 2010], indicating that the water ice signature observed by CRISM is most likely from surface frost. The lidar (light detection and ranging) instrument first observed nighttime water ice clouds at $L_s \sim 111°$ [*Whiteway et al.*, 2009]. After $L_s \sim 114°$, the nighttime 3.17/1.5 band depth ratio is consistently low, indicating that most of the ice absorptions are coming from surface ice (Figure 13). The SSI first observed frost on the surface on sol 79 ($L_s \sim 112°$) at ~0600 LTST. The next sol, it observed 0200 LTST frost on the telltale experiment, and afternoon (1300 LTST) frost in the shadows of large rocks (Figure 17). The low 3.17/1.5 band depth ratio and appearance of water ice absorptions lead us to conclude that the first water ice condenses on the surface in the nighttime between $L_s \sim 104°$ and 109°.

[45] We observed water ice form on the surface in the afternoon at $L_s \sim 154°$, earlier than CRISM observations in the previous year [*Cull et al.*, 2010]. During the 2007 observing cycle, CRISM first observed afternoon (1500 LTST) water ice on the surface at $L_s \sim 167°$ [*Cull et al.*, 2010]; however, the 2007 observations were not directly over the Phoenix landing site – most were 1–2 degrees below the landing site. Phoenix SSI images first show evidence of afternoon (1300 LTST) water ice in the shadows of large rocks on operations sol 80 ($L_s \sim 112°$; Figure 17). Ice was also observed later in the mission on the shadowed walls of trenches. Presumably, this is remnant ice from nighttime frost deposits. Ice does not appear to be stable on the sunlit surface until after $L_s \sim 154°$.

5. Conclusions

[46] Surface scattering parameters at the Phoenix landing site are well approximated by scattering parameters that also fit model observations of Gusev Crater soils [e.g., *Johnson et al.*, 2006], presumably because they are both dusty plains surfaces.

[47] Figure 18 summarizes the seasonal ice cycle at the Phoenix landing site based on CRISM and HiRISE observations prior to, during, and immediately after Phoenix operations, combined with Phoenix ground measurements by the SSI, OM, and lidar instruments.

[48] 1. During late spring and early summer ($L_s \sim 59°$ to ~109°), the surface is ice-free. The continued presence of a 3 μm water band during this time period indicates the surface is hydrated, probably by a thin layer of water adsorbed onto surface grains.

[49] 2. Permanent patches of water ice in the shadowed sides of Heimdal and large mountains to the northeast exist throughout the summer, and do not appreciably grow or shrink. The permanent ices darken between $L_s \sim 119°$ and $L_s \sim 160°$, possibly due to the sublimation or sintering of fine-grained ices cold trapped onto the ice deposits during the spring defrost period.

[50] 3. CRISM observations indicate the first nighttime (0300 LTST) surface frosts form at $L_s \sim 109°$, consisting of fine-grained (~20 μm) water ices.

[51] 4. SSI onboard Phoenix saw the first early morning (0600 LTST) frosts at $L_s \sim 112°$.

[52] 5. Lidar onboard Phoenix saw the first nighttime water ice clouds at $L_s \sim 111°$ [*Whiteway et al.*, 2009]. Lidar did not observe daytime water ice clouds during operations ($L_s \sim 77°$ to ~149°).

[53] 6. CRISM observes the first afternoon (1300 LTST) water ice clouds form at $L_s \sim 157°$.

[54] 7. In 2007, CRISM observed the first afternoon (1300 LTST) water ice form on the surface at $L_s \sim 165°$ [*Cull et al.*, 2010]. In 2009, the first afternoon water ice formed on the surface sometime around $L_s \sim 156°$.

[55] 8. CRISM does not observe CO_2 frost form on the surface before CRISM observations cease at $L_s \sim 177°$, its final observation before the onset of the polar hood.

[56] **Acknowledgments.** We acknowledge support from NASA as part of the Phoenix and CRISM Science Teams. We would like to thank the CRISM and HiRISE teams for their Phoenix monitoring campaign and Hugh Kieffer and an anonymous reviewer for their insightful reviews.

References

Arvidson, R. E., J. L. Gooding, and H. J. Moore (1989), The Martian surface as imaged, sampled, and analyzed by the Viking Landers, *Rev. Geophys.*, *27*(1), 39–60, doi:10.1029/RG027i001p00039.

Arvidson, R. E., F. Poulet, J.-P. Bibring, M. Wolff, A. Gendrin, R. V. Morris, J. J. Freeman, Y. Langevin, N. Mangold, and G. Bellucci (2005), Spectral reflectance and morphologic correlations in eastern Terra Meridiani, Mars, *Science*, *307*(5715), 1591–1594, doi:10.1126/science.1109509.

Arvidson, R. E., et al. (2006), Overview of the Spirit Mars Exploration Rover mission to Gusev Crater: Landing site to Backstay Rock in the Columbia Hills, *J. Geophys. Res.*, *111*, E02S01, doi:10.1029/2005JE002499.

Arvidson, R. E., et al. (2009), Results from the Mars Phoenix Lander Robotic Arm experiment, *J. Geophys. Res.*, *114*, E00E02, doi:10.1029/2009JE003408.

Bass, D., and D. A. Paige (2000), Variability of Mars' north polar water ice cap: II. Analysis of Viking IRTM and MAWD data, *Icarus*, *144*, 397–409.

Bonitz, R. G., et al. (2008), NASA Mars 2007 Phoenix Lander Robotic Arm and Icy Soil Acquisition Device, *J. Geophys. Res.*, *113*, E00A01, doi:10.1029/2007JE003030.

Brown, A. J., et al. (2008), Louth Crater: Evolution of a layered water ice mound, *Icarus*, *196*, 433–445, doi:10.1016/j.icarus.2007.11.023.

Clancy, R. T., S. W. Lee, G. R. Gladstone, W. W. McMillan, and T. Rousch (1995), A new model for Mars atmospheric dust based upon analysis of ultraviolet through infrared observations from Mariner 9, Viking, and Phobos, *J. Geophys. Res.*, *100*, 5251–5263, doi:10.1029/94JE01885.

Clancy, R. T., M. J. Wolff, and P. R. Christensen (2003), Mars aerosol studies with the MGS TES emission phase function observations: Optical depths, particle sizes, and ice cloud types versus latitude and solar longitude, *J. Geophys. Res.*, *108*(E9), 5098, doi:10.1029/2003JE002058.

Conrath, B. J., J. C. Pearl, M. D. Smith, W. C. Maguire, P. R. Christensen, S. Dason, and M. S. Kaelberer (2000), Mars Global Surveyor Thermal Emission Spectrometer (TES) observations: Atmospheric temperatures during aerobraking and science phasing, *J. Geophys. Res.*, *105*, 9509–9519, doi:10.1029/1999JE001095.

Cull, S. C., et al. (2010), Seasonal H_2O and CO_2 ices at the Mars Phoenix landing site: Results from prelanding CRISM and HiRISE observations, *J. Geophys. Res.*, *115*, E00D16, doi:10.1029/2009JE003340.

Eluszkiewicz, J. (1993), On the microphysical state of the Martian polar caps, *Icarus*, *103*, 43–48, doi:10.1006/icar.1993.1056.

Gaffey, S. J., et al. (1997), Ultraviolet, visible, and near-infrared reflectance spectroscopy: Laboratory spectra of geologic minerals, in *Remote Geochemical Analysis: Elemental and Mineralogical Composition*, edited by C. M. Pieters and P. A. J. Englert, pp. 43–71, Cambridge Univ. Press, Cambridge, U. K.

Hapke, B. (1981), Bidirectional reflectance spectroscopy: 1. Theory, *J. Geophys. Res.*, *86*, 3039–3054, doi:10.1029/JB086iB04p03039.

Hapke, B. (1993), *Theory of Reflectance and Emittance Spectroscopy*, Cambridge Univ. Press, Cambridge, U. K., doi:10.1017/CBO9780511524998.

Hecht, M. H., et al. (2008), Microscopy capabilities of the Microscopy, Electrochemistry, and Conductivity Analyzer, *J. Geophys. Res.*, *113*, E00A22, doi:10.1029/2008JE003077.

Heet, T. L., R. E. Arvidson, S. C. Cull, M. T. Mellon, and K. D. Seelos (2009), Geomorphic and geologic settings of the Phoenix Lander mission landing site, *J. Geophys. Res.*, *114*, E00E04, doi:10.1029/2009JE003416.

Henyey, L. G., and J. L. Greenstein (1941), Diffuse radiation in the galaxy, *Astrophys. J.*, *93*, 70–83, doi:10.1086/144246.

James, P. B., et al. (1993), The seasonal cycle of carbon dioxide on Mars, in *Mars*, edited by H. Kieffer, pp. 934–968, Univ. of Ariz. Press, Tucson.

Johnson, J. R., et al. (1999), Preliminary results on photometric properties of materials at the Sagan Memorial Station, Mars, *J. Geophys. Res.*, *104*, 8809–8830, doi:10.1029/98JE02247.

Johnson, J. R., et al. (2006), Spectrophometric properties of materials observed by Pancam on the Mars Exploration Rovers: 1. Spirit, *J. Geophys. Res.*, *111*, E02S14, doi:10.1029/2005JE002494.

Jouglet, D., F. Poulet, R. E. Milliken, J. F. Mustard, J.-P. Bibring, Y. Langevin, B. Gondet, and C. Gomez (2007), Hydration state of the Martian surface as seen by Mars Express OMEGA: 1. Analysis of the 3 μm hydration feature, *J. Geophys. Res.*, *112*, E08S06, doi:10.1029/2006JE002846.

Kieffer, H. H., and T. N. Titus (2001), TES mapping of Mars' northern seasonal cap, *Icarus*, *154*, 162–180, doi:10.1006/icar.2001.6670.

Langevin, Y., J.-P. Bibring, F. Montmessin, F. Forget, M. Vincendon, S. Douté, F. Poulet, and B. Gondet (2007), Observations of the south seasonal cap of Mars during recession in 2004–2006 by the OMEGA visible/near-infrared imaging spectrometer on board Mars Express, *J. Geophys. Res.*, *112*, E08S12, doi:10.1029/2006JE002841.

Milliken, R. E., J. F. Mustard, F. Poulet, D. Jouglet, J.-P. Bibring, B. Gondet, and Y. Langevin (2007), Hydration state of the Martian surface as seen by Mars Express OMEGA: 2. H_2O content of the surface, *J. Geophys. Res.*, *112*, E08S07, doi:10.1029/2006JE002853.

Moore, H. J., et al. (1987) Physical properties of the surface materials at the Viking landing sites on Mars, *U.S. Geol. Surv. Prof. Pap.*, *1389*.

Murchie, S., et al. (2007), Compact Reconnaissance Imaging Spectrometer for Mars (CRISM) on Mars Reconnaissance Orbiter (MRO), *J. Geophys. Res.*, *112*, E05S03, doi:10.1029/2006JE002682.

Pelkey, S. M., et al. (2007), CRISM multispectral summary products: Parameterizing mineral diversity on Mars from reflectance, *J. Geophys. Res.*, *112*, E08S14, doi:10.1029/2006JE002831.

Poulet, F., Y. Langevin, G. Boubin, D. Jouglet, J.-P. Bibring, and B. Gondet (2008), Spectral variability of the Martian high latitude surfaces, *Geophys. Res. Lett.*, *35*, L20201, doi:10.1029/2008GL035450.

Roush, T. L. (1994), Charon: More than water ice?, *Icarus*, *108*, 243–254, doi:10.1006/icar.1994.1059.

Seelos, K. D., et al. (2008), Geomorphologic and mineralogic characterization of the northern plains of Mars at the Phoenix Mission candidate landing sites, *J. Geophys. Res.*, *113*, E00A13, doi:10.1029/2008JE003088.

Smith, M. D. (2002), The annual cycle of water vapor on Mars as observed by the Thermal Emission Spectrometer, *J. Geophys. Res.*, *107*(E11), 5115, doi:10.1029/2001JE001522.

Smith, M. D. (2004), Interannual variability in TES atmospheric observations of Mars during 1999–2003, *Icarus*, *167*, 148–165, doi:10.1016/j.icarus.2003.09.010.

Smith, P. H., et al. (2008), Introduction to special section on the Phoenix mission: Landing site characterization experiments, mission overviews, and expected science, *J. Geophys. Res.*, *113*, E00A18, doi:10.1029/2008JE003083.

Smith, P. H., et al. (2009), Water at the Phoenix landing site, *Science*, *325*, 58–61, doi:10.1126/science.1172339.

Stamnes, K., et al. (1988), Numerically stable algorithm for discrete-ordinate-method radiative transfer in multiple-scattering and emitting layered media, *Appl. Opt.*, *27*, 2502–2509, doi:10.1364/AO.27.002502.

Tamppari, L. K., et al. (2010), Phoenix and MRO coordinated atmospheric measurements, *J. Geophys. Res.*, *115*, E00E17, doi:10.1029/2009JE003415.

Warren, S. G. (1984), Optical constants of ice from the ultraviolet to the microwave, *Appl. Opt.*, *23*, 1206–1225, doi:10.1364/AO.23.001206.

Whiteway, J. M., et al. (2009), Mars water ice clouds and precipitation, *Science*, *325*(5936), 68–70, doi:10.1126/science.1172344.

Wiseman, S., et al. (2007), Initial analysis of CRISM data over Meridiani Planum, *Lunar Planet. Sci.*, *XXXVIII*, Abstract 1945.

Wiseman, S., et al. (2009), Spectral and stratigraphic mapping of hydrated sulfate and phyllosilicate-bearing deposits: Implications for the aqueous history of Sinus Meridiani, Mars, Ph.D. dissertation, Washington Univ. in St. Louis, St. Louis, Mo.

Wolff, M. J., et al. (2007), Some studies of Martian aerosol properties using MRO/CRISM and MRO/Marci, in *Seventh International Conference on Mars, July 9–13, 2007, Pasadena CA* [CD-ROM], *LPI Contrib.*, 1353, Abstract 3121.

Wolff, M. J., M. D. Smith, R. T. Clancy, R. E. Arvidson, M. Kahre, F. Seelos IV, S. Murchie, H. Savijarvi, and the CRISM Science Team (2009), Wavelength dependence of dust aerosol single scattering albedo as observed by the Compact Reconnaissance Imaging Spectrometer, *J. Geophys. Res.*, *114*, E00D04, doi:10.1029/2009JE003350.

R. E. Arvidson and S. Cull, Department of Earth and Planetary Sciences, Washington University in Saint Louis, Saint Louis, MO 63112, USA.

M. T. Lemmon, Department of Atmospheric Science, Texas A&M University, College Station, TX 77843, USA.

M. T. Mellon, Laboratory for Atmospheric and Space Physics, University of Colorado at Boulder, Boulder, CO 80309, USA.

R. V. Morris, ARES, NASA Johnson Space Center, Houston, TX 77058, USA.

M. Wolff, Space Science Institute, 4750 Walnut St., Ste. 205, Boulder, CO 80301, USA.